RSC Advances

PAPER

View Article Online
View Journal | View Issue

Cite this: *RSC Adv.*, 2024, **14**, 22792

NIR afterglow nanosystem for photodynamic therapy†

Bingxin Shu,[a] Shubi Zhao,[b] Yuling Zhang,[a] Qinchao Sun*[b] and Zhen Huang*[c]

Received 5th May 2024
Accepted 19th June 2024

DOI: 10.1039/d4ra03312d

rsc.li/rsc-advances

Within the milieu of immune dysfunction, reactive oxygen species (ROS) play a pivotal role in inducing immunogenic cell death (ICD), countering the dysregulated tumor microenvironment. However, the administration of ROS at indiscriminate dosages may provoke deleterious immune responses. Therefore, precise regulation of ROS production is crucial to achieve efficacious therapeutic outcomes. We engineered an innovative afterglow nanosystem which is capable of real-time monitoring of ROS levels. Our findings reveal that Ru/CYQ@CPPO exhibits a markedly enhanced and prolonged afterglow luminescence, coupled with superior singlet oxygen (O_2) generation, compared to the commercially available indocyanine green (ICG). *In vitro* studies demonstrated that Ru/CYQ@CPPO exhibits remarkable efficacy in photodynamic therapy (PDT) under irradiation at a wavelength of 450 nm. Furthermore, a significant correlation ($R^2 = 0.987$) was observed between the intensity of afterglow luminescence and the rate of cancer cell inhibition.

1. Introduction

For several decades, apoptosis was predominantly viewed as a non-immunogenic or tolerogenic phenomenon. In stark contrast, necrotic cell death, including necroptotic apoptosis, has been acknowledged as a critical factor in driving inflammatory and immune responses. Recently, the emergent concept of 'immunogenic cell death' (ICD) has significantly challenged this conventional perspective, attributing immunogenic properties to apoptotic processes.[1] The model was originally conceptualized within the framework of anticancer chemotherapy, specifically aimed at enhancing the immunogenicity of cancer cells in response to an immunologically impaired microenvironment.[2,3] ICD-associated immunogenicity is more effectively enhanced through reactive oxygen species (ROS)-based therapies, including photodynamic and hemodynamic therapies. This enhancement is primarily due to the induction of ICD by ROS, which are generated as a result of endoplasmic reticulum (ER) stress.[4] In the tumor microenvironment, the precise modulation of ROS levels is crucial for inducing ICD. An optimal dosage of ROS facilitates this process, whereas deviations, either in excess or insufficiency, prove to be counterproductive.[5] Employing fluorescence imaging as a technique to elucidate the process of ROS generation presents a promising strategy for quantifying ROS levels in biological systems. This approach could significantly enhance our understanding and monitoring of ROS-mediated therapeutic mechanisms in cancer treatment. Nevertheless, real-time photoexcited fluorescence imaging is compromised by tissue autofluorescence, which adversely impacts the signal-to-background ratio (SBR) and *in vivo* sensitivity. This challenge can be effectively addressed through afterglow luminescence, also known as persistent luminescence, which is characterized by sustained autofluorescence following the termination of external light excitation.[6]

Molecule-based sustained luminescence has become an emerging field. The term "sustained luminescence" refers to luminescence that includes decay, long afterglow, persistence and long lifetime. Due to their delayed emission, materials with sustained luminescence have historically been used in emergency signs and dark luminescent paints found in watches.[7,8] In addition, these materials have been used for *in vivo* bioimaging because their time-resolved light signals reduce background interference. In contrast to co-crystals and/or hybrid crystals assembled at the molecular level, doped and co-mingled hybrid materials are aggregates of organic particles and/or micro/nanostructures with different chemical compositions. Doping photophores in organic compounds is a promising and easily accessible method of hybridisation, which reduces energy dissipation and immobilises the photophores by inhibiting molecular motion and intermolecular collisions. Molecular design controls the emission properties of doped materials, making organic materials potential candidates for many

---

[a] Shenzhen Clinical Medical College, Guangzhou University of Chinese Medicine, Shenzhen 518172, Guangdong, China

[b] Research Laboratory for Biomedical Optics and Molecular Imaging, Shenzhen Institutes of Advanced Technology, Chinese Academy of Sciences, Shenzhen 518055, Guangdong, China. E-mail: qchao.sun@siat.ac.cn

[c] Department of Laboratory Medicine of Pingshan District Maternal & Child Healthcare Hospital, Shenzhen 518122, Guangdong, China. E-mail: 635999667@qq.com

† Electronic supplementary information (ESI) available. See DOI: https://doi.org/10.1039/d4ra03312d

biomedical applications.[9,10] Afterglow imaging holds significant promise for ultrasensitive biomedical applications, primarily due to its ability to detect photons subsequent to the cessation of real-time photoexcitation. This unique capability facilitates the effective elimination of autofluorescence, a common challenge in imaging techniques. Despite its potential, the development of afterglow imaging remains nascent, hindered by the scarcity of afterglow agents that possess reliable lifetimes, biocompatibility, and high luminescence intensity. This limitation is particularly pronounced in the near-infrared spectrum, which is crucial for *in vivo* applications.[11] To date, a limited number of small-molecule organic materials capable of emitting afterglow have been documented, alongside a selection of inorganic persistent luminescent nanoparticles.[12,13] In recent years, much attention has been paid to the research of organic afterglow materials. There are several types of organic afterglow systems that have been developed, such as: phenylenevinylene (PPV),[14] thioether,[15] Schaap's dioxetanes,[16] and porphyrins (Fig. S1†).[17] Characteristically, these organic afterglow materials offer notable benefits, including high biosafety, effective biodegradability, and versatile surface functionalization options.[18,19] Organic afterglow materials offer great opportunities to overcome the above barriers to inorganic afterglow materials for *in vivo* bioimaging due to their biocompatible components and flexible designability.

In our research, we have developed a novel Near Infrared (NIR) afterglow nanosystem $Ru(bpy)_3^{2+}$/CYQ@CPPO (Ru/CYQ@CPPO) with dual-cycle amplification of the afterglow signal for visualising ROS generation during ROS-mediated cancer therapy. The afterglow intensity of Ru/CYQ@CPPO was enhanced by the generated $^1O_2$ *via* a dual-cycle amplification pathway, effectively inducing apoptosis in cancer cells. Moreover, a reasonable correlation between the intensity of the afterglow signals and the inhibition of cell growth was found. In summary, our synthesized afterglow probes offer an innovative approach for real-time prediction of therapeutic outcomes in $^1O_2$-mediated cancer therapy.

2. Experimental section

2.1 Materials

$Ru(bpy)_3^{2+}$ (purity ≥ 99%) were purchased from Macklin Inc. (Shanghai, China), 1,3-diphenylisobenzofuran (DPBF, purity ≥98%), TWEEN®80 (purity: for cell culture) and bis-(3,4,6-trichloro-2-(pentyloxycarbonyl)phenyl)oxalate (CPPO, purity ≥98%) were purchased from Aladdin biological technology Co. Ltd (Shanghai, China), Singlet Oxygen Sensor Green (SOSG) were purchased from invitrogen by Thermo Fisher Scientific Inc. Bis(2-ethylhexyl) sebacate (DOS, purity ≥97%) were purchased from aladdin (Shanghai, China). Tetrahydrofuran (THF, purity ≥99.5%) were purchased from Shanghai Lingfeng Chemical Reagents Co., Ltd, trisbuffer were purchased from Sigma-Aldrich (Shanghai, China). Dulbecco's modified Eagle's medium (DMEM) and Penicillin/Streptomycin (PS) were purchased from HyClone (Shanghai, China). Phosphate-buffered solution (PBS) was purchased from Corning (Shanghai, China). Trypsin–EDTA was purchased from Gibco (New York, USA). HeLa cells were provided by Research Center for Biomedical Optics and Molecular Imaging in the Shenzhen Institute of Advanced Technology, Chinese Academy of Science. Cell Counting Kit-8 (CCK-8) was purchased from Dojindo Chemical Technology Co., Ltd (Shanghai, China).

Dynamic light scattering (DLS) was measured on Zetasizer Nano ZS (Malvern, UK). The absorbance was recorded by on UV-2700 Spectrophotometer (SHIMADZU, Japan). The fluorescent spectra were recorded by using an Infinite M1000 PRO fluorometer (Tecan). The fluorescent and afterglow luminescence images of centrifuge tube were obtained *via* an IVIS spectrum imaging system (PerkinElmer).

2.2 Synthesis of CYQ and CYQI

Synthesis of CYQ and CYQI was reported previously (Fig. S2 and S3†).[20,21]

2.3 Characterizations of NIR dyes

CYQ, CYQI and ICG dissolved in THF. The UV-Vis absorption spectrum was determined by UV-2700 Ultraviolet-Visible Spectrophotometer (SHIMADZU, Japan). Zetasizer Nano ZS (Malvern, UK) was used to study the size distribution and zeta potential of Ru/CYQ @CPPO by DLS.

2.4 Synthesis of various near-infrared afterglow fluorescent probes

For screening of NIR fluorescent dyes, various NIR fluorescent dyes (*e.g.*, ICG, CYQ or CYQI) were prepared by dissolving them separately in tetrahydrofuran (THF).

To synthesis of Ru/CYQ@CPPO: different amounts of CYQ, different amounts of Ru, 10 μL of DOS and 5 μL of Tween-80 were mixed thoroughly. First, 10 μL of DOS was added to a 1.5 mL EP tube, and after adding different microlitres of Ru and CYQ in turn, it was mixed thoroughly, then 5 μL of Tween-80 was added, and it was slowly blown at least 60 times. Finally, the Ru/CYQ@CPPO NIR afterglow probe was prepared by dropping the mixture in the EP tube into 1 mL of PBS in a vortex. (If not mixed well in the EP tube, it will be prepared as a cloudy liquid, and a successful preparation should be a green, translucent liquid.)

Single linear oxygen yield assay: ICG, CYQ, and CYQI were weighed into 100 μM and diluted for UV-Vis measurement, adjusted to OD = 10. The 165 μL of SOSG was added to the trisbuffer and dissolved, and 10 μL of SOSG was added to 990 μL of trisbuffer. The 200 μL of trisbuffer, 10 μL of SOSG, and 10 μL (ICG, CYQ, or CYQI) were mixed with or without laser irradiation for 5 min, and then the fluorescence intensity was measured. Take 200 μL of trisbuffer, 10 μL of SOSG, and 10 μL of ICG, CYQ, or CYQI, and then measure the fluorescence intensity with or without irradiating the laser for 5 min.

2.5 Measurement of single linear state oxygen quantum yield (ΦΔ)

The single linear state oxygen quantum yield (ΦΔ) was measured by detecting the change in absorption of DPBF (1,3-

diphenylisobenzofuran) at 410 nm, with ICG as the reference photosensitizer.[22,23] An air-saturated DPBF (100 μM) methanol solution containing the photosensitizer was irradiated using a laser light source at 660 nm, and measurements were taken every 60 seconds of irradiation. Absorption spectra were measured using a UV-visible spectrometer. ΦΔ values were obtained by the relative value method in the following equation:

$$\Phi\Delta = \Phi\Delta(\mathrm{Std})\frac{S_{\mathrm{PS}} \times F_{\mathrm{Std}}}{S_{\mathrm{Std}} \times F_{\mathrm{PS}}} \tag{1}$$

where the subscripts PS and Std denote CYQ and ICG, respectively, and S denotes the slope of the curve obtained by plotting the change in absorption value of DPBF at 410 nm relative to the light time. F denotes the absorption correction factor, $F = 1-10^{-\mathrm{OD}}$ (OD stands for absorbance at 660 nm), and the laser power is 10 mW cm^{-2}.

2.6 Optimal conditions for the preparation of near-infrared afterglow fluorescent probes

To optimize the doping of CYQ, Ru/CYQ@CPPO was doped with different concentrations of CYQ and irradiated with a laser (450 nm, 0.75 W cm^{-2}) for 2 min before afterglow imaging (Ru: 0.2 mg mL^{-1}, CYQ: 0, 0.1, 0.2, 0.4 mg mL^{-1}).

To optimize the doping of Ru, Ru/CYQ@CPPO was doped with different concentrations of Ru (0.04, 0.1, and 0.2 mg mL^{-1}) and irradiated with a laser (450 nm, 0.75 W cm^{-2}) for 2 min prior to afterglow imaging (CYQ: 0.2 mg mL^{-1}, Ru: 0, 0.04, 0.1, 0.2 mg mL^{-1}).

2.7 Stability of near-infrared afterglow fluorescent probes

To study the duration of afterglow intensity after irradiation, the afterglow fluorescence intensity was recorded at one-minute intervals for 5 minutes after irradiation of Ru/CYQ@CPPO with a laser (450 nm, 0.75 W cm^{-2}).

In order to study the afterglow intensity after cyclic irradiation, the afterglow intensity was recorded as 0 before laser irradiation. Ru/CYQ@CPPO was irradiated with a laser (450 nm, 0.75 W cm^{-2}), which was recorded once after 1 min laser irradiation. Then, the photons were freely released for 10 minutes and re-recorded. Then, four cycles were repeated, and data were recorded.

2.8 Cell culture and cellular experiments

HeLa cells were cultured in DMEM supplemented with 10% FBS (fetal bovine serum) and antibiotics (10 U mL^{-1} penicillin and 10 mg mL^{-1} streptomycin) at 37 °C containing 5% CO_2.

HeLa cells were inoculated in 96-well plates and incubated with fresh DMEM. After 24 hours of incubation, the medium in the 96-well plates was replaced with medium containing Ru/CYQ@CPPO (final concentrations: 0, 3.125, 12.5, 25, 50, 100 μg mL^{-1}) and incubated for another 3 hours. These cells were then subjected to 2 min of laser (450 nm, 0.75 W cm^{-2}) irradiation or no light irradiation and further incubated for 24 hours. Finally, relative cell viability was tested using the CCK-8 assay.

2.9 Statistical analysis

All experimental data were expressed as mean ± standard deviation, and SPSS 16.0 statistical software was used for data analysis. P value <0.05 was considered statistically significant.

3. Results

3.1 The photophysical properties of NIR dyes

Three NIR organic dyes were investigated for the potential candidate of the afterglow nanosystem. A commercially available dye ICG was taken as reference for the characterization of other two novel cyanine dyes. As shown in Fig. 1a, the two heavy atoms of iodine were introduced to CYQI to increase the intersystem crossing probability.

To verify that we successfully synthesised the NIR dyes, we first tested the absorption peaks. The absorption spectra of CYQ, CYQI, and ICG were a characterized as shown in Fig. 1b. The absorption maximum of CYQ, CYQI were found to be around 816 nm and 796 nm, which were red-shifted in comparison to that of ICG 784 nm. In order to investigate the triplet state of those three dyes, the $^1O_2$ generation experiments were conducted, as shown in Fig. 1c and d. SOSG was taken as the $^1O_2$ probe to indicate the generation of $^1O_2$ *via* the fluorescence intensity variation around 530 nm. As shown in Fig. 1c, the SOSG fluorescence exhibits a pronounced increase in the presence of CYQ after laser irradiation at 785 nm, registering a fourfold enhancement compared to pre-irradiation. In

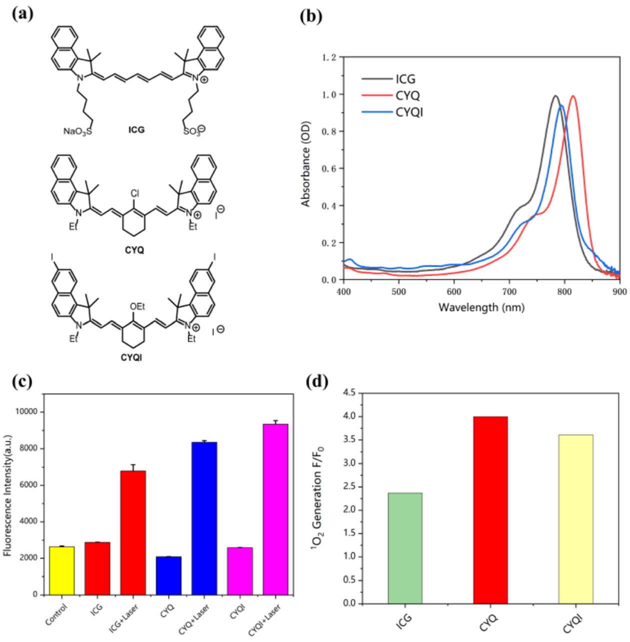

Fig. 1 Screening of organic dyes for afterglow nanosystem. (a) Molecular structures of NIR fluorescent dyes (ICG, CYQ, CYQI). (b) Absorption spectra of ICG, CYQ, and CYQI. (c) The fluorescence intensity of SOSG in the presence of different dyes with and without laser irradiation (785 nm, 0.75 W cm^{-2}, 5 min), data were presented as means ± SD ($n = 10$). (d) SOSG fluorescence enhancement (F/F_0) for different NIR fluorescent dyes after laser irradiation.

contrast, in the case of ICG a much lower emission intensity was observed. It indicates a higher $^1O_2$ generation was found for CYQ than the commercially available dye ICG. Given CYQ's superior $^1O_2$ generation efficiency, it was selected for further investigation. Given CYQ's superior $^1O_2$ generation efficiency, it was selected for further investigation.

In photodynamic therapy, the generation of $^1O_2$ plays a crucial role in eradicating tumor cells. Consequently, the quantum yield of $^1O_2$ is considered to be a critical parameter for evaluating the efficacy of photosensitizers. It is pivotal in determining the therapeutic potential and efficiency of photodynamic treatments.[24,25] In our study, we quantified the relative $^1O_2$ quantum yield of CYQ by employing 1,3-diphenylisobenzofuran (DPBF) as a scavenger for $^1O_2$ and ICG as a reference photosensitizer. The DPBF would be oxidized by the produced reactive oxygen species leads to a reduction in the absorbance around 410 nm.[26] As shown in Fig. 2a–c, by irradiation at 785 nm, the absorbance band of DPBF getting lower as a function of time. The quantum yield of $^1O_2$ generation was about $\Phi\Delta_{(CYQ)} = 0.106$, which is 0.9 times that of ICG (Fig. 2). A *K*-value of CYQ, ICG, and DPBF were 0.99×10^{-2}, 1.03×10^{-2}, and 0.35×10^{-2}, respectively (Fig. 2d).

3.2 Enhanced afterglow luminescence with chemiluminescent substrates

The widely accepted luminescence mechanism of organic afterglow-emitting nanoparticles is that after the afterglow material receives light irradiation, the afterglow initiator generates ROS, which reacts with the material to form unstable high-energy intermediates, and the continuous luminescence can be delayed after the unstable decomposition.[27] Though the CYQ could generate a certain amount of $^1O_2$ after irradiation at 785 nm, the quantum yield is too low in comparison to the famous Ru $(bpy)_3^{2+}$ compound. The triplet state quantum yield is considered to be unity.[28] Therefore, we applied $Ru(bpy)_3^{2+}$ as afterglow initiator, for which after irradiation at 450 nm, the energy would be used to convert bis-(3,4,6-trichloro-2-(pentyloxycarbonyl)phenyl)oxalate (CPPO) into a high-energy dioxetanedione intermediate. This intermediate, in turn, excites the adjacent CYQ molecules, thereby significantly amplifying the afterglow intensity. This proposed mechanism underscores a novel pathway for enhancing luminescent efficiency in photodynamic applications. In this study, we successfully prepared Ru/CYQ@CPPO nanosystem. A uniform distribution of CPPO within the Ru/CYQ matrix, potentially leads to an improved performance (Fig. 3a). To verify that the nanosystem is a nanomaterial, we tested the DLS. The DLS of Ru/CYQ@CPPO showed its hydrodynamic diameter to be around 86.61 (±6.59) nm and positively charged (Fig. 3b and S4†). To achieve the most effective afterglow luminescence, we conducted a comprehensive study to fine-tune the concentration of each species in the Ru/CYQ@CPPO nanosystem. In order to obtain the best afterglow nanosystem, we synthesized various Ru/CYQ@CPPO, while maintaining a constant CYQ/CPPO concentration ratio. The results indicated that the nanosystem with 2 mg mL^{-1} CPPO and 0.2 mg mL^{-1} CYQ demonstrated the highest afterglow intensity. This observation suggests an optimal doping ratio within these parameters for enhanced

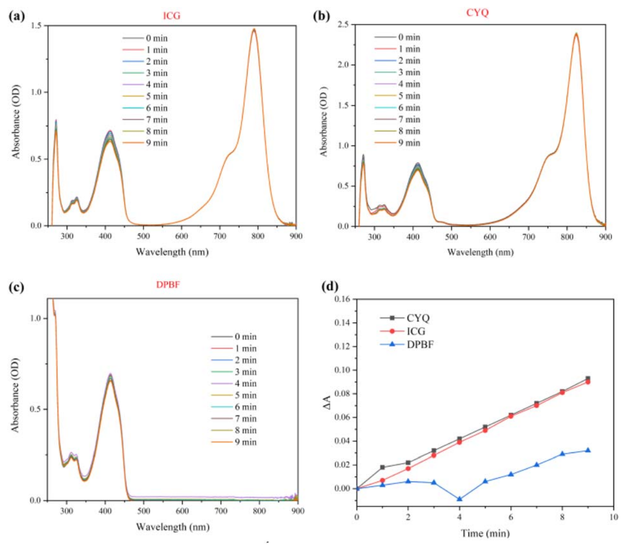

Fig. 2 The measurement of $^1O_2$ quantum yield of ICG and CYQ *via* the absorption change of DPBF. The absorption spectra variation of DPBF as a function of irradiation time in methanol in the presence of ICG (a), CYQ (b), and DPBF (c). (d) The change of absorbance of DPBF at 410 nm as a function of irradiation time. Irradiated at 660 nm with intensity of 10 mW cm^{-2}.

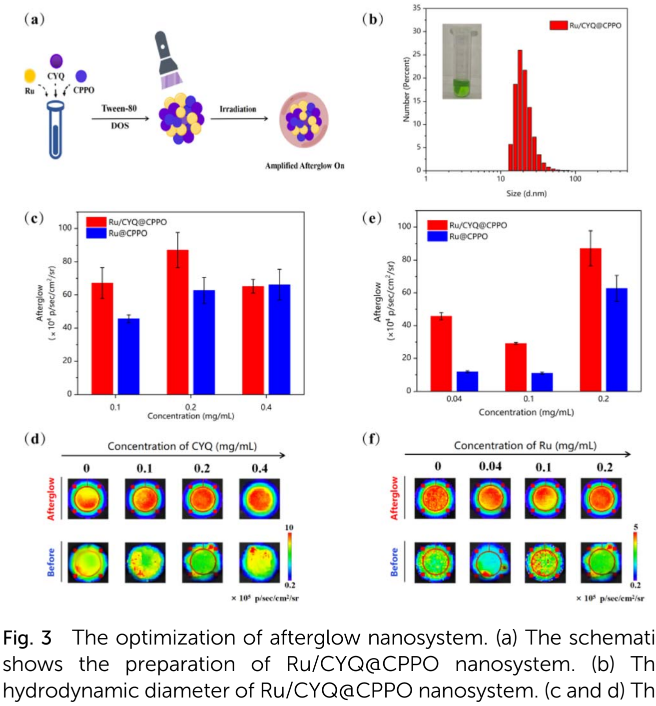

Fig. 3 The optimization of afterglow nanosystem. (a) The schematic shows the preparation of Ru/CYQ@CPPO nanosystem. (b) The hydrodynamic diameter of Ru/CYQ@CPPO nanosystem. (c and d) The afterglow intensity of Ru/CYQ@CPPO at different CYQ concentrations after irradiation with at 450 nm, 0.75 W cm^{-2} (Ru: 0.2 mg mL^{-1}, CYQ: 0, 0.1, 0.2, 0.4 mg mL^{-1}), data were presented as means ± SD ($n = 3$). (e and f) The afterglow intensity of Ru/CYQ@CPPO at different concentrations of Ru after irradiation with 450 nm, 0.75 W cm^{-2} (CYQ: 0.2 mg mL^{-1}, Ru: 0, 0.04, 0.1, 0.2 mg mL^{-1}).

afterglow performance in these composites (Fig. 3c and d). In addition, the afterglow intensity of Ru/CYQ@CPPO was 4 times higher than that of Ru@CPPO when the doping of Ru is 0.04 mg mL^{-1} (Fig. 3e and f).

The kinetics of afterglow intensity of Ru@CPPO, CYQ@CPPO, and Ru/CYQ@CPPO after laser excitation were investigated as shown in Fig. 4a. Notably, the NIR afterglow intensity of Ru/CYQ@CPPO exhibited a progressive increase post-irradiation, with reaching maximum around one minute. Remarkably, even in its diminished state, the afterglow intensity of Ru/CYQ@CPPO remained significantly higher compared to that of other control samples (Fig. 4a). This observation suggests that Ru and CYQ exhibit a synergistic effect following laser irradiation, significantly amplifying the afterglow intensity. Furthermore, the afterglow recharge properties of Ru/CYQ@CPPO was examined as shown in Fig. 4b and c. Surprisingly, the afterglow intensity would be increased dramatically as increasing the recharge cycle. It might be caused by the accumulating of the charged CPPO during each afterglow cycle.

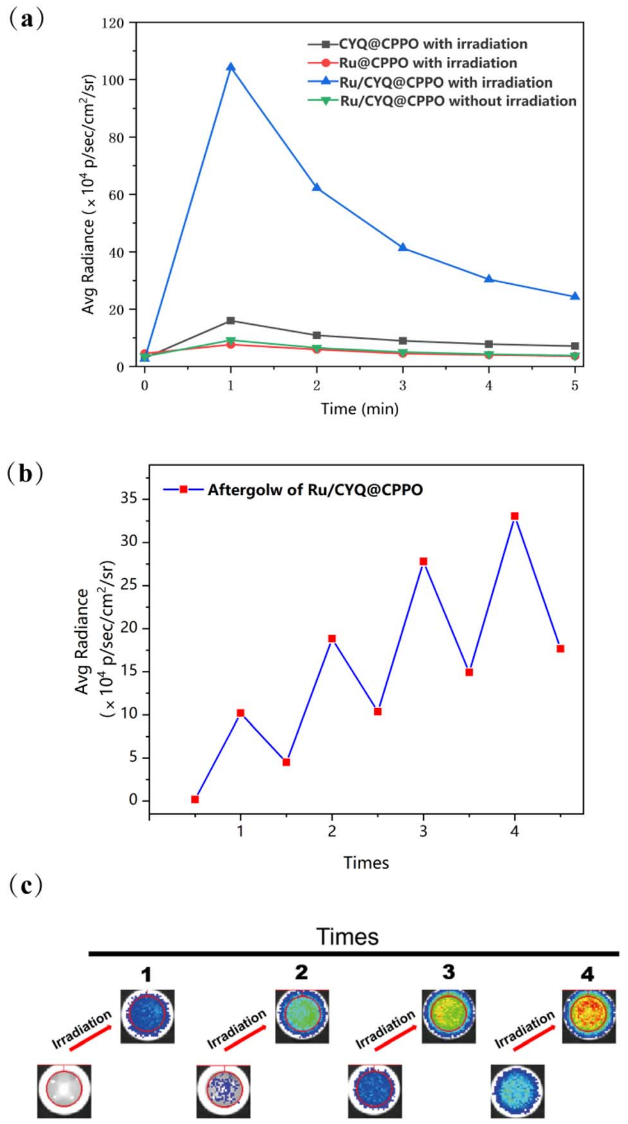

Fig. 4 The kinetics of afterglow nanosystem. (a) The afterglow of Ru/CYQ@CPPO after irradiation at 450 nm. (b and c) Afterglow intensities and images of Ru/CYQ@CPPO as a function of irradiation cycles. The nanosystem were in dark for 10 min after each irradiation cycle.

3.3 *In vitro* anticancer efficiency

The impact of ROS on immunogenic responses exhibits considerable variability, primarily contingent upon the ROS dosage produced during photodynamic therapy.[29–31] Consequently, the unpredictable generation of ROS by therapeutic agents could potentially elicit detrimental effects on anti-tumor immunity, thereby rendering the treatment process a significant source of adverse side effects. The growing interest in monitoring ROS production during ICD-related immunotherapy is noteworthy. This study was motivated by the observed correlation between NIR afterglow luminescence and the production of $^1O_2$. Therefore, we explored the relationship between the NIR afterglow intensity of Ru/CYQ@CPPO in solution and ($^1O_2$) generation, as illustrated in Fig. 5a. In Fig. 5b, we demonstrate a marked enhancement in the afterglow intensity of Ru/CYQ@CPPO, which is proportional to its concentration as laser irradiated. The photodynamic therapeutic efficacy of HeLa cells were investigate *via* incubation with varying concentrations of Ru/CYQ@CPPO, as shown in Fig. 5c. The corresponding afterglow signals were quantitatively captured using the IVIS live animal imaging system, as shown in Fig. 5b. With increasing the incubation concentration of Ru/CYQ@CPPO, a gradual enhancement in the afterglow intensity was observed in the cells. Furthermore, a corresponding decreasing in cell viability was also recorded *via* employing the CCK-8 assay, as shown in Fig. 5c. A reasonable correlation (R^2 =

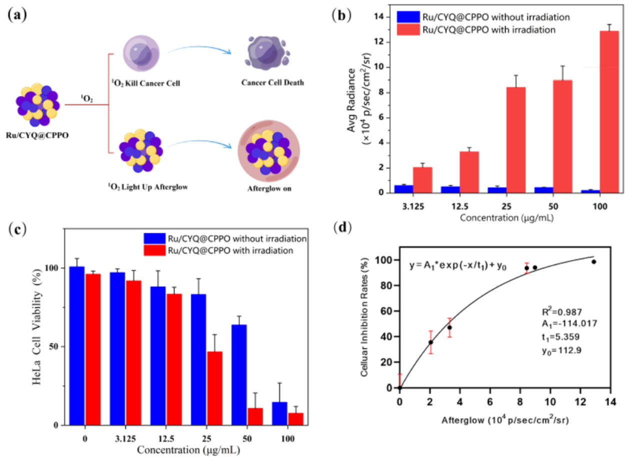

Fig. 5 Afterglow nanosystem for *in vitro* study. (a) The scheme of $^1O_2$ generation and afterglow monitoring associated with photodynamic therapy. (b) Afterglow intensity (with and without laser irradiation) of different concentrations of Ru/CYQ@CPPO (450 nm, 0.75 W cm^{-2}), data were presented as means ± SD (n = 3). (c) Relative viability of HeLa cells incubated with different concentrations of Ru/CYQ@CPPO (with or without laser irradiation) 450 nm, 0.75 W cm^{-2}, data were presented as means ± SD (n = 4). (d) Correlation between afterglow intensity and tumor cell inhibition was calculated using the data in (b) and (c).

0.987) was established between the afterglow intensity and cell inhibition, as presented in Fig. 5d. As the afterglow signal corresponds to $^1O_2$ concentration, which is also directly correlated to the degree of tumor inhibition. Therefore the Ru/CYQ@CPPO afterglow nanosystem presents an effective nanoprobe, which facilitates real-time assessment of therapeutic efficacy *via* NIR afterglow during photodynamic therapy.

4. Conclusions

We developed a novel near-infrared afterglow nanosystem Ru/CYQ@CPPO. It is composed by Ru $(bpy)_3^{2+}$ as the afterglow initiator, CYQ as the substrate, and CPPO as the afterglow enhancer and relay component. The nanoparticle size of Ru/CYQ@CPPO is consistently within the range of 80–100 nm. The Ru/CYQ@CPPO nanosystem has passive targeting to tumor tissues, leveraging the enhanced permeability and retention (EPR) effect.[32] The Ru/CYQ@CPPO exhibits a strong afterglow and a robust recharging effect. Furthermore, a reasonable correlation between the intensity of afterglow luminescence and the inhibition rate of tumor cells was established, which indicates that the Ru/CYQ@CPPO nanosystem holds promise for facilitating non-invasive, personalized PDT, offering a predictive measure for the efficacy of PDT treatments.

Data availability

All relevant data are within the manuscript and its additional files. The data are available from the corresponding author on reasonable request.

Author contributions

Bingxin Shu: methodology; formal analysis; investigation; writing-original draft. Shubi Zhao: methodology; formal analysis; investigation; writing-original draft. Yuling Zhang: formal analysis; investigation; Qinchao Sun: conceptualization; resources; supervision; funding acquisition; validation; writing-review and editing. Zhen Huang: supervision; funding acquisition; validation; writing-review and editing. Bingxin Shu, Shubi Zhao & Yuling Zhang contributed equally to this work.

Conflicts of interest

The authors declare that they have no known competing financial interests or personal relationships that could have appeared to influence the work reported in this paper.

Acknowledgements

This work was supported by the National Natural Science Foundation of China (No. 22077135, No. 21905296, No. 22377142).

References

1 A. Serrano-Del Valle, A. Anel, J. Naval, I. Marzo, A. Serrano-Del Valle, A. Anel, J. Naval and I. Marzo, Immunogenic Cell Death and Immunotherapy of Multiple Myeloma, *Front. Cell Dev. Biol.*, 2019, **7**, 50.

2 M. Hu, J. Zhang, L. Kong, Y. Yu, Q. Hu, T. Yang, Y. Wang, K. Tu, Q. Qiao, X. Qin and Z. Zhang, Immunogenic Hybrid Nanovesicles of Liposomes and Tumor-Derived Nanovesicles for Cancer Immunochemotherapy, *ACS Nano*, 2021, **15**(2), 3123–3138.

3 G. Kroemer, L. Galluzzi, O. Kepp and L. Zitvogel, Immunogenic cell death in cancer therapy, *Annu. Rev. Immunol.*, 2013, **31**, 51–72.

4 W. Li, J. Yang, L. Luo, M. Jiang, B. Qin, H. Yin, C. Zhu, X. Yuan, J. Zhang, Z. Luo, Y. Du, Q. Li, Y. Lou, Y. Qiu and J. You, Targeting photodynamic and photothermal therapy to the endoplasmic reticulum enhances immunogenic cancer cell death, *Nat. Commun.*, 2019, **10**(1), 3349.

5 H. Deng, W. Yang, Z. Zhou, R. Tian, L. Lin, Y. Ma, J. Song and X. Chen, Targeted scavenging of extracellular ROS relieves suppressive immunogenic cell death, *Nat. Commun.*, 2020, **11**(1), 4951.

6 Y. Wang, G. Song, S. Liao, Q. Qin, Y. Zhao, L. Shi, K. Guan, X. Gong, P. Wang, X. Yin, Q. Chen and X. B. Zhang, Cyclic Amplification of the Afterglow Luminescent Nanoreporter Enables the Prediction of Anti-cancer Efficiency, *Angew. Chem., Int. Ed.*, 2021, **60**(36), 19779–19789.

7 R. Gao, M. S. Kodaimati and D. Yan, Recent advances in persistent luminescence based on molecular hybrid materials, *Chem. Soc. Rev.*, 2021, **50**(9), 5564–5589.

8 B. Hou, B. Zheng, W. Yang, C. Dong, H. Wang and J. Chang, Construction of near infrared light triggered nanodumbbell for cancer photodynamic therapy, *J. Colloid Interface Sci.*, 2017, **494**, 363–372.

9 G. Xiao, Y. J. Ma, Z. Qi, X. Fang, T. Chen and D. Yan, A flexible ligand and halogen engineering enable one phosphor-based full-color persistent luminescence in hybrid perovskitoids, *Chem. Sci.*, 2024, **15**(10), 3625–3632.

10 B. Zheng, Y. Bai, H. Chen, H. Pan, W. Ji, X. Gong, X. Wu, H. Wang and J. Chang, Near-Infrared Light-Excited Upconverting Persistent Nanophosphors *in Vivo* for Imaging-Guided Cell Therapy, *ACS Appl. Mater. Interfaces*, 2018, **10**(23), 19514–19522.

11 W. Chen, Y. Zhang, Q. Li, Y. Jiang, H. Zhou, Y. Liu, Q. Miao and M. Gao, Near-Infrared Afterglow Luminescence of Chlorin Nanoparticles for Ultrasensitive *In Vivo* Imaging, *J. Am. Chem. Soc.*, 2022, **144**(15), 6719–6726.

12 S. He, C. Xie, Y. Jiang and K. Pu, An Organic Afterglow Protheranostic Nanoassembly, *Adv. Mater.*, 2019, **31**(32), e1902672.

13 W.-T. Huang, V. Rajendran, M.-H. Chan, M. Hsiao, H. Chang and R.-S. Liu, Near-Infrared Windows I and II Phosphors for Theranostic Applications: Spectroscopy, Bioimaging, and Light-Emitting Diode Photobiomodulation, *Adv. Opt. Mater.*, 2023, **11**, 2202061.

14 C. Xie, X. Zhen, Q. Miao, Y. Lyu and K. Pu, Self-Assembled Semiconducting Polymer Nanoparticles for Ultrasensitive Near-Infrared Afterglow Imaging of Metastatic Tumors, *Adv. Mater.*, 2018, **30**(21), e1801331.

15 S. Liao, Y. Wang, Z. Li, Y. Zhang, X. Yin, S. Huan, X. B. Zhang, S. Liu and G. Song, A novel afterglow nanoreporter for monitoring cancer therapy, *Theranostics*, 2022, **12**(16), 6883–6897.

16 A. P. Schaap, M. Sandison and R. S. Handley, Chemical and enzymatic triggering of 1,2-dioxctancs. 3: alkaline phosphatase-catalyzed chemiluminescence from an acryl phosphate-substituted dioxetane, *Tetrahedron Lett.*, 1987, **28**(11), 1159–1161.

17 X. Duan, G. Q. Zhang, S. Ji, Y. Zhang, J. Li, H. Ou, Z. Gao, G. Feng and D. Ding, Activatable Persistent Luminescence from Porphyrin Derivatives and Supramolecular Probes with Imaging-Modality Transformable Characteristics for Improved Biological Applications, *Angew. Chem., Int. Ed.*, 2022, **61**(24), e202116174.

18 P. Das, S. Ganguly, A. Rosenkranz, B. Wang, J. H. Yu, S. Srinivasan and A. R. Rajabzadeh, MXene/0D nanocomposite architectures: Design, properties and emerging applications, *Mater. Today Nano*, 2023, **24**, 100428.

19 P. Das, S. R. Ahmed, S. Srinivasan and A. R. Rajabzadeh, Optical Properties of Quantum Dots, in *Quantum Dots and Polymer Nanocomposites*, CRC Press, Boca Raton, FL, USA, 2022, vol. 4, pp. 69–85.

20 Z. Chang, L. J. Liu, J. Y. Zhai, C. C. Liu, X. Wang, C. B. Liu, X. J. Xie and Q. C. Sun, Molecular Electronic Coupling-Induced Photoacoustics for NIR-I/II Duplex *in Vivo* Imaging, *Chem. Mater.*, 2023, **35**(3), 1335–1344.

21 M. Cui, M. Ono, H. Kimura, H. Kawashima, B. L. Liu and H. Saji, Radioiodinated benzimidazole derivatives as single photon emission computed tomography probes for imaging of β-amyloid plaques in Alzheimer's disease, *Nucl. Med. Biol.*, 2011, **38**(3), 313–320.

22 Y. Wan, G. Lu, W. C. Wei, Y. H. Huang, S. Li, J. X. Chen, X. Cui, Y. F. Xiao, X. Li, Y. Liu, X. M. Meng, P. Wang, H. Y. Xie, J. Zhang, K. T. Wong and C. S. Lee, Stable Organic Photosensitizer Nanoparticles with Absorption Peak beyond 800 Nanometers and High Reactive Oxygen Species Yield for Multimodality Phototheranostics, *ACS Nano*, 2020, **14**(8), 9917–9928.

23 J. A. Cardillo, R. Jorge, R. A. Costa, S. M. Nunes, D. Lavinsky, B. D. Kuppermann, A. C. Tedesco and M. E. Farah, Experimental selective choriocapillaris photothrombosis using a modified indocyanine green formulation, *Br. J. Ophthalmol.*, 2008, **92**(2), 276–280.

24 Z. Lv, H. Wei, Q. Li, X. Su, S. Liu, K. Y. Zhang, W. Lv, Q. Zhao, X. Li and W. Huang, Achieving efficient photodynamic therapy under both normoxia and hypoxia using cyclometalated Ru(ii) photosensitizer through type I photochemical process, *Chem. Sci.*, 2017, **9**(2), 502–512.

25 R. Gao, X. Mei, D. Yan, R. Liang and M. Wei, Nano-photosensitizer based on layered double hydroxide and isophthalic acid for singlet oxygenation and photodynamic therapy, *Nat. Commun.*, 2018, **9**(1), 2798.

26 S. Sicwetsha, O. Adeniyi and P. Mashazi, Bimetallic gold and palladium nanoparticles supported on copper oxide nanorods for enhanced H_2O_2 catalytic reduction and sensing, *RSC Adv.*, 2021, **11**(46), 28818–28828.

27 H. Shen, S. Liao, Z. Li, Y. Wang, S. Huan, X. B. Zhang and G. Song, Organic Afterglow Nanoparticles in Bioapplications, *Chemistry*, 2023, **29**(42), e202301209.

28 R. T. Jukes, V. Adamo, F. Hartl, P. Belser and L. De Cola, Photochromic dithienylethene derivatives containing Ru(II) or Os(II) metal units. Sensitized photocyclization from a triplet state, *Inorg. Chem.*, 2004, **43**(9), 2779–2792.

29 B. Ji, M. Wei and B. Yang, Recent advances in nanomedicines for photodynamic therapy (PDT)-driven cancer immunotherapy, *Theranostics*, 2022, **12**(1), 434–458.

30 R. Alzeibak, T. A. Mishchenko, N. Y. Shilyagina, I. V. Balalaeva, M. V. Vedunova and D. V. Krysko, Targeting immunogenic cancer cell death by photodynamic therapy: past, present and future, *Immunother. Cancer*, 2021, **9**(1), e001926.

31 T. Jin, D. Cheng, G. Jiang, W. Xing, P. Liu, B. Wang, W. Zhu, H. Sun, Z. Sun, Y. Xu and X. Qian, Engineering naphthalimide-cyanine integrated near-infrared dye into ROS-responsive nanohybrids for tumor PDT/PTT/chemotherapy, *Bioact. Mater.*, 2021, **14**, 42–51.

32 M. Mahmoudi, S. Sant, B. Wang, S. Laurent and T. Sen, Superparamagnetic iron oxide nanoparticles (SPIONs): development, surface modification and applications in chemotherapy, *Adv. Drug Delivery Rev.*, 2011, **63**(1–2), 24–46.